Construction and Application of a Technical Platform for Determining Cell Cycle- and Autophagy-Associated Cellular Uptake of Lipid-Based Nanoparticles

Yisha Wang[1,2†], Gan Luo[1,2†], Haiyang Wang[1,2†], Yue Zheng[1,2], Wenbin Zhou[1,2], Junrong Lin[1,2], Baocheng Chen[1,2], Meihua Sui[1,2*]

[1]*School of Basic Medical Sciences, Zhejiang University School of Medicine, Hangzhou, China*

[2]*Cancer Center, Zhejiang University, Hangzhou, China*

†Equal contribution

[*]Corresponding author

Meihua Sui, M.D., Ph.D. **E-mail**: suim@zju.edu.cn

Abstract

Cellular uptake of biomedical nanoparticles has been shown to be affected by key cellular biological properties. However, very little is known about the influence of cell cycle and autophagy on nanoparticle uptake. What's even more tough is that several long-lasting methodological barriers hamper the experimental performance and restrict the research and development. Herein, a multi-functional platform was initially constructed for simultaneously overcoming existing obstacles by integrating several technical approaches, particularly mitotic shake-off, for scatheless and complete cell cycle phase separation. Strikingly, further application of this platform revealed that G2-phase and M-phase cells, two cell populations previously muddled up together as G2/M-phase cells, respectively exhibited the maximum and minimum uptake of lipid-based nanoparticles. Moreover, our data generally provided a novel line of evidence for enhanced nanoparticle uptake by specific autophagy blockade. The cell cycle- and autophagy-associated characteristics of nanoparticle uptake discovered here offer new insights for optimization and application of nanomedicines.

Leveraging the distinctive surface and size effect, nanodrugs have a wide range of applications in biomedicine[1]. Among a variety of nanocarriers, lipid-based nanoparticles, e.g. liposomes (LIP) and lipid nanoparticles (LNP), serve as exemplary carriers for successful clinical translation[2]. For instance, Doxil®, doxorubicin utilizing LIP as the carrier, is the first nano-sized drug approved for patients[3]. BNT162b2, the first LNP-delivered mRNA vaccine, is extensively used worldwide[4]. It has been noted that nanoparticle uptake could be affected by key cellular biological properties. Cell cycle, a fundamental life process of mammalian cells, is critically involved in the onset, development, treatment response and prognosis of many diseases[5]. Particularly, proliferating tumor cells inside tumor tissues are distributed at different cell cycle phases, which is called cell cycle heterogeneity[6,7]. Given that studies from our team and others demonstrate that tumor cells possess cell cycle-dependent sensitivity to a variety of treatments including nano-drugs, cell cycle heterogeneity has been considered as a big challenge for antitumor therapy[6-12].

Nevertheless, so far only three literatures explored the impact of cell cycle on the uptake of inorganic nanoparticles including CdTe QDs[13,14] and ZnO[15]. Regarding organic nanoparticles, five literatures respectively investigated the cell cycle-associated uptake of carboxylated polystyrene nanoparticles (PS-CCOH), FITC-dextran fibroin-encapsulated microspheres, cRGD-targeting matrix metalloproteinase-sensitive nanoparticles (FITC@NPs-cRGD), folate modified poly (L-amino acid) micelles and Tat/pGL3-Ca^{2+} nanoparticles[16-20]. It is noteworthy that several methodological limitations may interfere with the accuracy of data and result in the discrepant findings previously reported. For instance, the methods used or available in literatures could not differentiate between G2-phase and M-phase cells in physiological state[13-20]. Additionally, cell dissociation agent such as trypsin[13,15-19], exogenous stimuli (e.g., serum deprivation)[16,18] and “cell cycle blockers” (e.g., nocodazole)[13,15,18-20] for artificial synchronization of cell cycle, inevitably disturbed the cellular physiology and subsequent nanoparticle uptake. Moreover, evaluation of nanoparticle uptake with confocal laser scanning microscopy (CLSM) was limited at a two-dimensional (2D) level, in which spatial cellular architecture and heterogeneous intracellular distribution of nanoparticles were both ignored[13,17,19,20]. Indeed, these technical barriers have become "bottleneck" problems preventing deeper and further investigations in related research and development.

Autophagy is another major biological process involved in the maintenance of physiological homeostasis and pathogenesis of a wide range of diseases[21]. Interestingly, recent studies indicate that cancer cells are more dependent on autophagy than normal cells, with high levels of endogenous

autophagy detected in various types of cancers such as osteosarcoma and pancreatic cancer[22,23]. Evolutionarily conserved autophagy-related genes (*ATG* genes) are core regulatory genes of autophagy[21,24]. Moreover, endosomal/lysosomal system, which is critically involved in nanoparticle uptake[25], also plays a pivotal role in autophagy[26]. As a result, there is a growing body of related reports, with the majority focusing on the possible capability of nanoparticles to induce autophagy per se[27]. Up to date three literatures explored the potential effect of autophagy on cellular uptake of nanoparticles, including polystyrene[28,29] and silver[30] nanoparticles all measured at 2D level. Considering that non-specific autophagy inhibitors was used to modulate autophagy in these studies, the obtained data might be confounded by non-autophagy-related pharmacological effects induced by these non-specific inhibitors[31].

This study was inspired by our strong curiosities on the impact of cell cycle and endogenous autophagy on cellular uptake of nanoparticles, and by the methodological challenges existed in research on "nano-cell cycle/autophagy" interactions. Herein, a pair of isogenic cancer cell lines including wild type (WT) strain and *ATG7* knockout (*ATG7* KO) derivative was applied to eliminate the interferences caused by non-specific autophagy inhibitors. Importantly, by cleverly combining transfection of cell cycle indicator plasmid PIP-FUCCI[32] and mitotic shake-off[33], an alive, complete and scatheless distinguishment of four cell cycle phases was successfully achieved. Encouragingly, further integration with high-resolution CLSM and three-dimensional (3D) reconstruction technique enabled multi-dimensional evaluations on nanoparticle uptake. Through construction and application of this multi-functional platform, the influence of cell cycle and endogenous autophagy on cellular uptake of LIP of Doxil® and LNP of BNT162b2, two most widely used nanoparticles, were parallelly and systemically evaluated.

Synthesis and characterization of model nanoparticles DiD-LIP and DiD-LNP

Despite the wide application of LIP and LNP as drug carriers, our understandings on their "nano-bio" interactions are far from sufficient. So far, no literature has investigated the potential impact of either cell cycle or autophagy on the cellular uptake of LIP or LNP. Hereby LIP and LNP were respectively synthesized according to officially published formulations[34,35] and our previous report[4], with DiD as a tracer fluorescence[36,37]. Briefly, DiD-LIP was formulated by hydrating a lipid mixture containing HSPC, cholesterol, $mPEG_{2000}$-DSPE and DiD in sucrose-histidine buffer, followed by downsizing using a 10-mL extruder barrel (Fig. 1a left). DiD-LNP was prepared with a microfluidic mixing

device through mixing the ethanol phase containing ALC-0315, DSPC, cholesterol, ALC-0159, DiD and the aqueous phase containing firefly luciferase mRNA to enhance the stability of LNP[4,38] (Fig. 1a right).

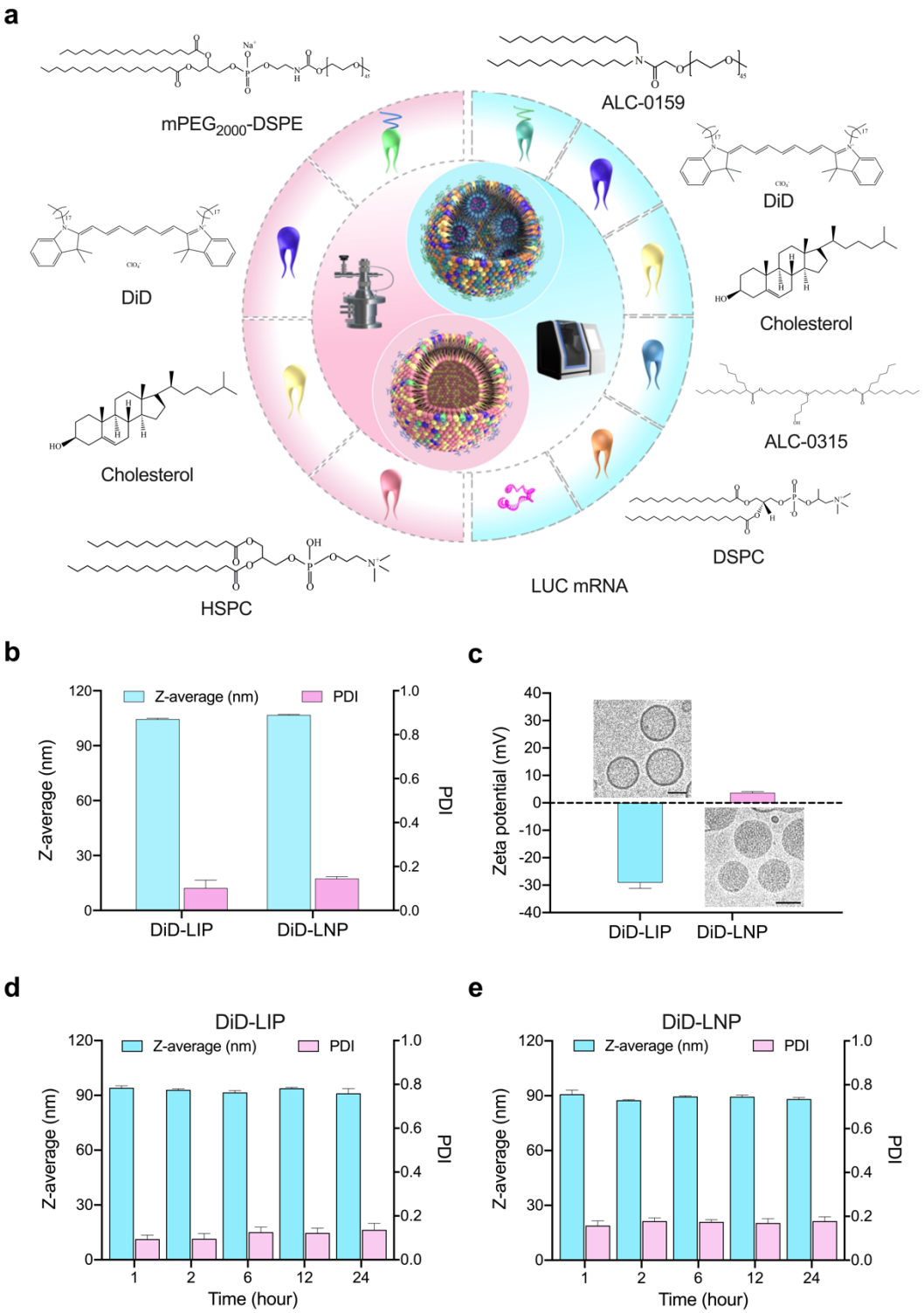

Fig. 1. Preparation and characterization of DiD-labelled liposomes (DiD-LIP) and lipid nanoparticles (DiD-LNP). a, Schematic illustration of the synthesis of DiD-LIP (left, pink background) and DiD-LNP (right, blue background). Briefly, to synthesis DiD-LIP, the sucrose-histidine buffer hydrated mPEG$_{2000}$-DSPE, DiD, cholesterol and HSPC to generate multilamellar vesicles, followed by size reduction through a 10-mL extruder barrel. To synthesize DiD-LNP, the ethanol phase dissolving ALC-0159, DiD, cholesterol, ALC-0315 and DSPC

was mixed with the aqueous phase containing firefly luciferase mRNA (LUC mRNA) at a flow rate ratio of 1: 3 (ethanol: aqueous) via a microfluidic mixing device. **b-c**, Z-average, polydispersity index (PDI), Zeta potentials and representative Cryo-TEM images (inserts) of DiD-LIP and DiD-LNP. Scale bars, 50 nm. **d-e**, Z-average and PDI of DiD-LIP and DiD-LNP in DMEM containing 10% FBS stored at 37 °C for up to 24 hours. Data in **b-e** were presented as "mean ± standard deviation" of three independent experiments. Z-average and PDI among various time points were evaluated by ANOVA with Bonferroni correction, with no statistically significant difference detected (all $P > 0.05$).

Further characterization with dynamic light scattering (DLS) showed that the Z-average/PDI of DiD-LIP and DiD-LNP were 104.433 ± 0.513 nm/0.102 ± 0.036 and 106.767 ± 0.306 nm/0.145 ± 0.009, respectively (Fig. 1b). Additional cryogenic transmission electron microscopy (Cryo-TEM) examination confirmed that DiD-LIP was characterized as hollow spheres, whereas DiD-LNP exhibited a typical electron-dense core structure containing mRNA (Fig. 1c, insert). Zeta potentials of DiD-LIP and DiD-LNP were -29.100 ± 2.081 mV and 3.660 ± 0.476 mV, respectively (Fig. 1c). These data demonstrate that both model nanoparticles possess highly monodisperse particle-size distribution and weak surface charge. Importantly, DiD-LIP and DiD-LNP exhibited good stability when stored in phosphate buffer saline at 4 °C, with no remarkable changes detected for Z-average or PDI from Day 1 to Day 28 (Supplementary Fig. 1a, b), or in cell culture medium containing 10% FBS at 37 °C for up to 24 hours (simulating the experimental environment) (Fig. 1d, e). Moreover, the standard curves of phospholipid and corresponding equations were obtained for further dosage determination of DiD-LIP and DiD-LNP (Supplementary Fig. 1c, d).

Establishment of a scatheless and multi-functional platform for determining cell cycle- and autophagy-associated cellular uptake of nanoparticles

Using empty vector as a control, the isogenic WT and *ATG7* KO U2OS cell lines previously constructed were transduced with lentiviral particles carrying the cell cycle-indicating PIP-FUCCI plasmid (see **Methods** section). After screening with G418 and flow cytometry, corresponding WT and *ATG7* KO PIP-FUCCI cell lines expressing strong mVenus (green fluorescence) and/or mCherry (red fluorescence) were obtained (Fig. 2a). PIP-FUCCI transfection and subsequent selection had marginal influence on cellular morphology and proliferation rate (Supplementary Figs. 2 and 3).

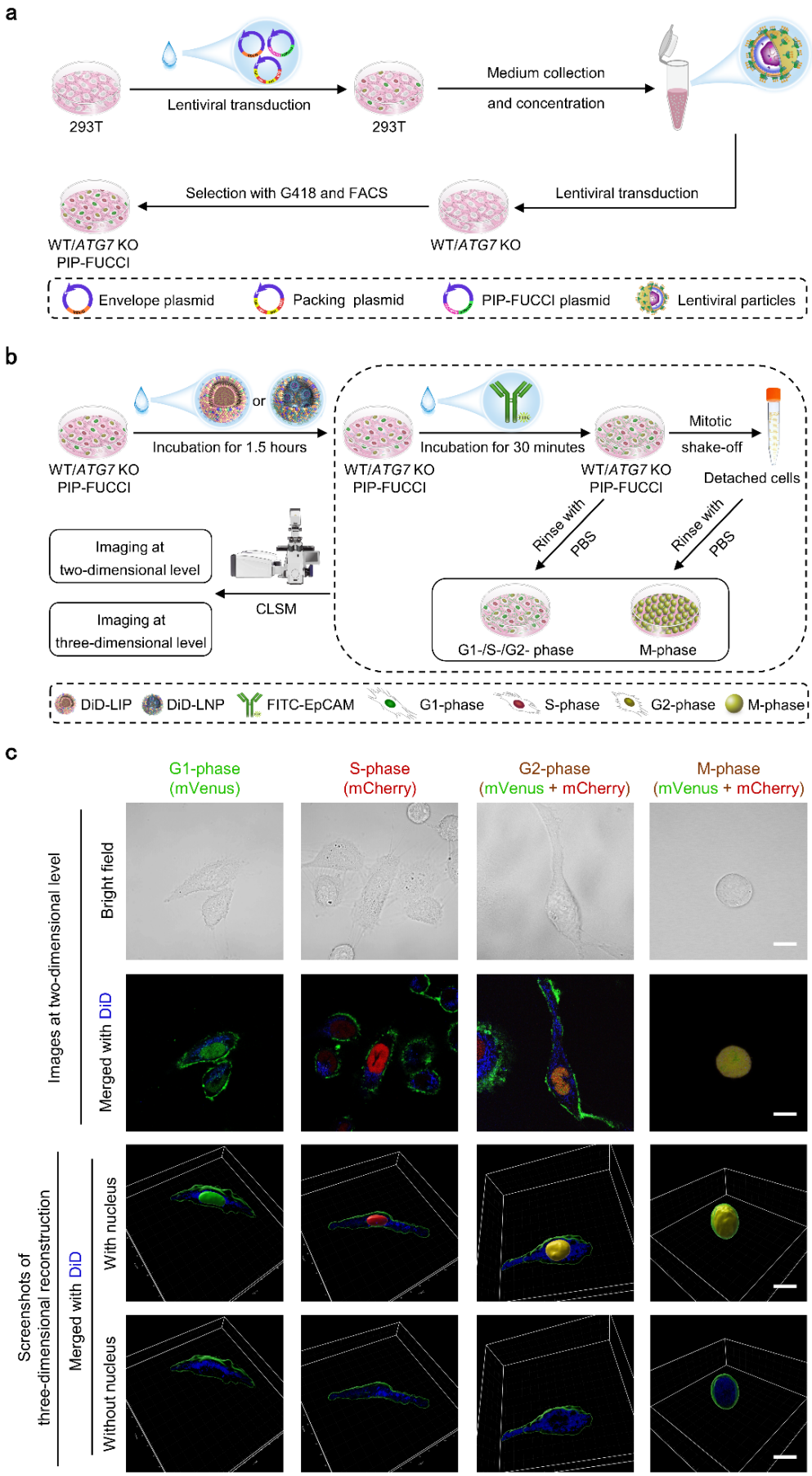

Fig. 2. Establishment of a scatheless and multi-functional technical platform for determining cell cycle- and autophagy-associated nanoparticle uptake. a, Schematic diagram shows the construction of cell lines stably

expressing PIP-FUCCI (cell cycle indicator) plasmid. Envelope plasmid PMD2.G, packing plasmid psPAX2 and transfer plasmid PIP-FUCCI were simultaneously added into 293T cells. Afterwards, the culture medium was collected and concentrated, followed by application of lentiviral supernatant containing PIP-FUCCI to isogenic wide type (WT) and *ATG7* knockout (*ATG7* KO) U2OS cell lines. Subsequently, WT and *ATG7* KO PIP-FUCCI cell lines stably expressing PIP-FUCCI were obtained after selection with G418 and flow cytometry (FACS). **b**, Schematic diagram indicates the establishment of a multi-functional platform for determining cell cycle- and autophagy-associated nanoparticle uptake. WT and *ATG7* KO PIP-FUCCI cells were treated with DiD-labelled liposomes (DiD-LIP, equivalent to 5 μg/mL DOX) or lipid nanoparticles (DiD-LNP, equivalent to 6 μg/mL luciferase mRNA) for 1.5 hours, followed by FITC-EpCAM incubation for 30 minutes to label cell membrane (green cell membrane). Complete distinguishment of cell cycle phase was cleverly achieved through combining PIP-FUCCI expression to indicate G1-phase (mVenus positive, green nucleus), S-phase (mCherry positive, red nucleus) and G2-phase (mVenus and mCherry double-positive, yellow nucleus) cells attached to culture dish, with mitotic shake-off to collect detached or floating M-phase cells (mVenus and mCherry double-positive, yellow nucleus). Further integration of confocal laser scanning microscope (CLSM) and three-dimensional reconstruction technique enabled detection and calculation of nanoparticle uptake at both two-dimensional and three-dimensional levels. c, Representative light microscopic and CLSM images demonstrating the successful construction and application of new technical platform, using DiD-LIP (blue fluorescence) and WT PIP-FUCCI cells as a model system. Scale bars, 20 μm.

However, although single positivity of mVenus and mCherry could respectively indicate cells at G1-phase and S-phase, both G2-phase and M-phase cells are mVenus and mCherry double-positive and exhibit yellow fluorescence (overlap of green and red). That is, PIP-FUCCI transfection by itself cannot distinguish between G2-phase and M-phase cells in situ. Fortunately, different from G1-phase, S-phase and G2-phase cells naturally adhering to culture dish with polyhedral shapes, typical M-phase cells have unique properties such as spherical shape[39] and significantly reduced adhesion capability or suspended state in culture media, leading to convenient collection of M-phase cells through gentle mitotic shake-off[33]. Enlightened by these characteristics, we skillfully combined PIP-FUCCI transfection with mitotic shake-off, through which a scatheless approach completely distinguishing four cell cycle phases was established. In addition, labeling cell membrane with FITC-EpCAM prior to mitotic shake-off helped to exclude apoptotic cells and cellular debris via drawing the outline of cell membrane (Fig. 2b, highlighted with dashed frame).

Further integration of high-resolution CLSM and 3D reconstruction technique significantly strengthened this multi-functional platform for determining cell cycle- and autophagy-associated cellular uptake of nanoparticles (Fig. 2b). Using DiD-LIP (blue fluorescence) as a representative, nanoparticle uptake was not only characterized at different dimensional levels, but respectively

evaluated at four different cell cycle phases in WT and *ATG7* KO PIP-FUCCI cells (Fig. 2c). In brief, this new platform has multiple superiorities including scatheless separation of alive cells at four cell cycle phases, elimination of interferences caused by "extra" treatments (e.g. cell dissociation agents, cell cycle synchronization drugs, none-specific autophagy inhibitors), and capability for parallel investigations on multiple biological parameters/dimensions.

Little influence of DiD-LIP and DiD-LNP per se on cell cycle progression and autophagy of WT and *ATG7* KO PIP-FUCCI cell lines

To clarify the impact of cell cycle and autophagy on nanoparticle uptake, the possible interference of model nanoparticles on cancer cells per se need to be firstly excluded. Therefore, WT and *ATG7* KO PIP-FUCCI cells were respectively treated with DiD-LIP and DiD-LNP for further evaluation. As depicted in Fig. 3a and Supplementary Table 1, flow cytometry analysis showed that cancer cells at G1-phase, S-phase and G2/M-phase were 28.75 ± 2.79%, 57.75 ± 2.14% and 13.50 ± 1.20%, respectively, for WT PIP-FUCCI cell line, and 26.95 ± 2.49%, 59.67 ± 0.51% and 13.38 ± 2.06%, respectively, for *ATG7* KO PIP-FUCCI cell line. Importantly, further statistical analysis demonstrated that no matter with or without nanoparticle treatment, no significant difference on cell cycle progression was observed in WT and *ATG7* KO PIP-FUCCI cells (Supplementary Table 2). Meanwhile, there was no statistical difference in cell cycle progression between WT and *ATG7* KO PIP-FUCCI cells (all $P > 0.05$). That is, neither nanoparticle treatment nor *ATG7* knockout affected the cell cycle progression.

Previous studies demonstrate that *ATG7* knockdown effectively blocked cellular autophagy[40]. Indeed, although autophagic vesicles (AVs, including autophagosomes and autophagic lysosomes) with typical double-layer membrane structure were easily observed in WT PIP-FUCCI cells with TEM, no typical AVs were seen in *ATG7* KO PIP-FUCCI cells (Fig. 3b). Further statistical analysis confirmed significantly fewer AVs in *ATG7* KO PIP-FUCCI cells than in WT PIP-FUCCI cells (Fig. 3c; Supplementary Table 3). As anticipated, ATG7 protein level was high in WT PIP-FUCCI cells while undetectable in *ATG7* KO PIP-FUCCI cells in Western blotting (Fig. 3d). Moreover, LC3-II/LC3-I ratio, which is positively correlated with the autophagy level[41], was significantly decreased in *ATG7* KO PIP-FUCCI cells. In contrast, p62, which is negatively correlated with autophagy[41], was dramatically increased in *ATG7* KO PIP-FUCCI cells. Our data firmly demonstrated the successful blockade of autophagy in *ATG7* KO PIP-FUCCI cells. Encouragingly, neither DiD-LIP nor DiD-LNP

exhibited any effect in aforementioned assays, indicating that designated nanoparticle treatment had marginal impact on the autophagy of WT and *ATG7* KO PIP-FUCCI cells.

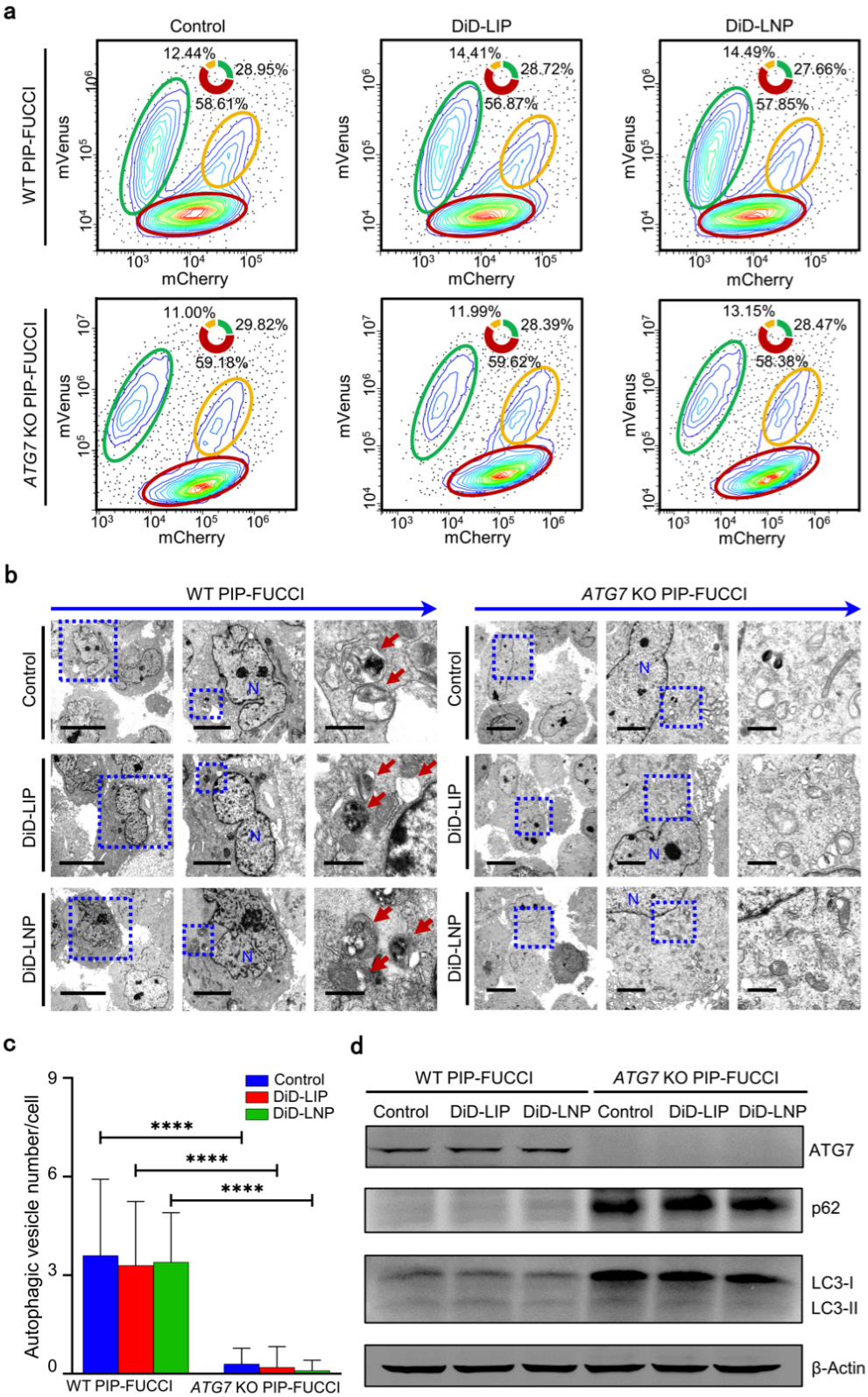

Fig. 3. Validation of cell cycle progression and endogenous autophagy in WT and *ATG7* KO PIP-FUCCI cells with or without nanoparticle treatment. a, Representative flow cytometry data on cell cycle progression. Cells accumulated at G1-phase, S-phase and G2/M-phase were respectively circled in green, red and orange, with the corresponding percentages indicated. **b**, Representative transmission electron microscope images of autophagic

vesicles indicated by rust-red arrows. N, nucleus. Scale bars, from left to right, 10 μm, 4 μm and 1 μm for WT PIP-FUCCI cells, and 10 μm, 3 μm and 1 μm for *ATG7* KO PIP-FUCCI cells. **c**, Statistical analysis of the autophagic vesicle number per cell. Data were presented as "mean ± standard deviation" (n = 10) and further analyzed by Mann-Whitney U test. ****, $P < 0.0001$. **d**, Representative western blot analysis of autophagy-related proteins including ATG7, p62 and LC3. WT PIP-FUCCI, wide type U2OS cells stably expressing PIP-FUCCI; *ATG7* KO PIP-FUCCI, *ATG7* knockout U2OS cells stably expressing PIP-FUCCI. DiD-labelled liposomes (DiD-LIP) and lipid nanoparticles (DiD-LNP) were administered to cancer cells at a dosage equivalent to 5 μg/mL DOX and a dosage equivalent to 6 μg/mL luciferase mRNA respectively) for 2 hours.

Determination of cell cycle- and endogenous autophagy-associated cellular uptake of DiD-LIP

Next, we meticulously captured abundant CLSM images with intracellular co-localization of cell cycle-indicating fluorescence and DiD-LIP using this new platform (Supplementary Videos 1-8; Supplementary Fig. 4). Subsequently, cell size, Total Fluorescence Intensity (TFI) and Mean Fluorescence Intensity (MFI) were respectively calculated and analyzed at 2D and 3D levels (Fig. 4; Table 1; Supplementary Tables 4 and 5). Our data showed that TFI (2D) of DiD-LIP across various cell cycle phases exhibited same characteristics in both cell lines, which was M < G1 ≈ S < G2. Further integration of 3D reconstruction technique revealed the following cell cycle-associated characteristics of TFI (3D) of DiD-LIP: M (≈ G1) < (G1 ≈) S < G2 in WT PIP-FUCCI cells; M < G1 < S < G2 in *ATG7* KO PIP-FUCCI cells.

As expected, both cell lines exhibited a gradual increase in cell area (2D level) upon cell cycle progressing from G1-phase to G2-phase, followed by a decrease at M-phase due to mitotic cell rounding to become spherical[42]. Consistent with previous reports, cell volume (3D level) gradually increased while cells sequentially going through G1-phase, S-phase, G2-phase and M-phase of the cell cycle[43,44]. Hereby MFI (2D) based on cell area and MFI (3D) based on cell volume were initially calculated and analyzed for additional exploration. Impressively, MFI (2D) and MFI (3D) of DiD-LIP exhibited same characteristics in both cell lines, which was M < G1 ≈ S ≈ G2. These data may suggest that the relatively higher increase in cell size of G2-phase cells attenuated the aforementioned difference in TFI detected between G2-phase and G1-phase/S-phase. Taken together, our study not only differentiated between G2-phase and M-phase cells in physiological state, but provided initial evidence that G2-phase and M-phase cells respectively absorbed the maximum and minimum nanoparticles. Interestingly, it has been suggested that M-phase cells have declined endocytosis and elevated cell membrane tension, which may assist mother cell to prevent external disturbances during

mitosis[45]. These properties support our findings that M-phase cells had minimum nanoparticle uptake among four cell cycle phases.

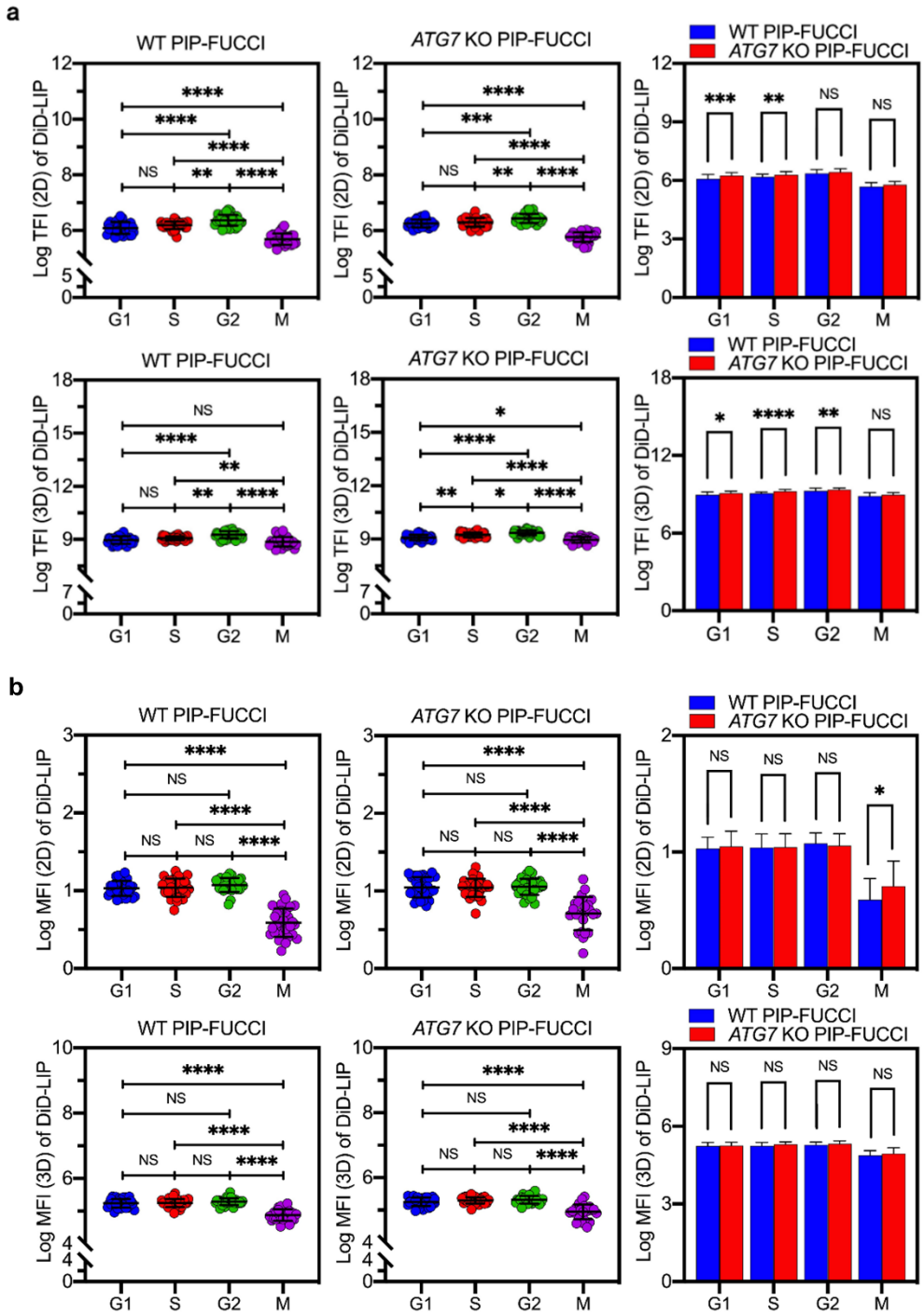

Fig. 4. Determination of cell cycle- and endogenous autophagy-associated cellular uptake of DiD-labelled liposomes (DiD-LIP) using the newly established technical platform. a, Statistical analysis of Total Fluorescence Intensity (TFI) in G1-phase, S-phase, G2-phase and M-phase WT and *ATG7* KO PIP-FUCCI cells respectively measured at two-dimensional (2D, upper panel) and three-dimensional (3D, lower panel) levels. **b**, Statistical analysis of Mean Fluorescence Intensity (MFI) in WT and *ATG7* KO PIP-FUCCI cells respectively measured at aforementioned four cell cycle phases, as well as at 2D (upper panel) and 3D (lower panel) levels. WT PIP-FUCCI, wide type U2OS cells stably expressing PIP-FUCCI; *ATG7* KO PIP-FUCCI, *ATG7* knockout U2OS cells stably expressing PIP-FUCCI. DiD-LIP was administered at a dosage equivalent to 5 μg/mL DOX for 2 hours. All data

were analyzed after $\log_{10}$ transformation and presented as "mean ± standard deviation" (n = 25-30). Statistical analysis of DiD-LIP uptake among four different cell cycle phases was conducted using ANOVA with Bonferroni correction, while differences between WT and *ATG7* KO PIP-FUCCI cell lines were evaluated with an independent sample *t*-test. *, $P < 0.05$; **, $P < 0.01$; ***, $P < 0.001$; ****, $P < 0.0001$. NS, not significant.

As mentioned above, discrepant results were reported in literatures investigating the influence of cell cycle on nanoparticle uptake[13-20]. For instance, although uptake of CdTe QDs[13,14], ZnO[15], PS-CCOH[16] and FITC–dextran fibroin-encapsulated microspheres[17] showed same cell cycle-associated characteristics (G2/M > S > G1), FITC@NPs-cRGD uptake exhibited a reverse ranking (G1 > S > G2/M). It should be noted that cells at G2-phase and M-phase were muddled up as G2/M-phase cells in most previous studies[13-19], except G2-phase and M-phase synchronizations were respectively induced using RO3306 and paclitaxel in one study[20].

Moreover, both TFI and MFI of DiD-LIP suggested an association between nanoparticle uptake and endogenous autophagy. For instance, TFI (2D) of G1-phase and S-phase *ATG7* KO PIP-FUCCI cells, TFI (3D) of G1-phase, S-phase and G2-phase *ATG7* KO PIP-FUCCI cells, as well as MFI (2D) of M-phase *ATG7* KO PIP-FUCCI cells, all exhibited significant increases and surpassed those of WT PIP-FUCCI cells. Previously there are three literatures explored the influence of autophagy on nanoparticle uptake, all of which using 2D fluorescence intensity for uptake assessment and non-specific autophagy inhibitors for autophagy inhibition: Fageria et al. reported a reduced cellular uptake of Ag nanoparticles upon chloroquine treatment[30]; Sipos et al. observed a suppressed cellular uptake of polystyrene nanoparticles after exposure to 3-methyladenine and bafilomycin A1[28,29]. However, different from *ATG7* knockout that specifically blocks endogenous autophagy, non-autophagy-related pharmacological effects such as induction of cell death and lysosomotropic activities have been reported for chloroquine, 3-methyladenine and bafilomycin A1, which may interfere with the cellular uptake of nanoparticles[46,47].

Determination of cell cycle- and endogenous autophagy-associated cellular uptake of DiD-LNP

WT and *ATG7* KO PIP-FUCCI cells were further treated with DiD-LNP and evaluated with the multi-functional platform (Fig. 5; Table 1; Supplementary Videos 9-16; Supplementary Fig. 5; Supplementary Tables 6 and 7). Impressively, TFI (2D) of DiD-LNP in both cell lines, and TFI (3D) and MFI (2D) of DiD-LNP in WT PIP-FUCCI cell line, all exhibited same characteristics as TFI (2D) of DiD-LIP, which was M < G1 ≈ S < G2. MFI (3D) in WT and TFI (3D) in *ATG7* KO PIP-FUCCI

cells showed similar characteristics, except G1 < S in WT and M ≈ G1 in *ATG7* KO PIP-FUCCI cells. Moreover, MFI (2D) and MFI (3D) in *ATG7* KO PIP-FUCCI cells were M < G1 ≈ S ≈ G2 and M < (G1 ≈) S < (G1 ≈) G2, respectively, coinciding with the aforementioned attenuation of differences between G2-phase and G1-phase/S-phase due to relatively higher increase in cell size of G2-phase cells. In general, multi-dimensional data obtained with DiD-LNP confirmed that G2-phase cells had maximum whereas M-phase cells had minimum nanoparticle uptake. Interestingly, we noted that mean values of TFI and MFI of two model nanoparticles exhibited similar tendency in both cell lines, which is M < G1 < S < G2. These data might imply that when proliferating cells progress into a new cell cycle with physiological activities such as cellular protein and DNA synthesis gradually intensifying, nanoparticle uptake becomes active in synchronization till the cells enter "circumspect" M-phase[48,49].

Moreover, it is noteworthy that M-phase cells have the minimum cell areas, which would weaken the difference of MFI (2D) between M-phase cells and cells at other phases. Nevertheless, M-phase cells of both cell lines still exhibited extremely significant decrease in MFI (2D) upon treatment with two model nanoparticles (nearly all $P < 0.0001$). In contrast, M-phase cells have the maximum cell volumes, which would strengthen the difference of MFI (3D) between M-phase cells and cells at other phases. It is thereby logical that the following significant differences in MFI (3D) arose, although no difference was detected with corresponding TFI (3D): M < G1 in MFI (3D) of DiD-LIP in WT PIP-FUCCI cells, M < G1 and M < S in MFI (3D) of DiD-LNP in *ATG7* KO PIP-FUCCI cells, all $P < 0.0001$.

Interestingly, different from DiD-LIP that exhibited several significantly higher TFI and MFI in *ATG7* KO PIP-FUCCI cells than those in WT PIP-FUCCI cells, DiD-LNP showed increased TFI but reduced MFI in *ATG7* KO PIP-FUCCI cells compared with WT strain. In detail, TFI (2D) of M-phase, and TFI (3D) of G1-phase and M-phase *ATG7* KO PIP-FUCCI cells were significantly higher than those of WT PIP-FUCCI cells. However, both MFI (2D) and MFI (3D) of S-phase and G2-phase *ATG7* KO PIP-FUCCI cells were significantly lower than those in WT strain. These data, together with Pearson correlation coefficient (Supplementary Tables 8-11) indicate that TFI (2D), TFI (3D), MFI (2D) and MFI (3D) are correlated but different parameters whose usefulness warrant further evaluation. As 3D assessment offers a more comprehensive consideration of various factors, e.g. morphological changes during cell cycle progression (particularly between M-phase and other phases), disparities in cellular volume[43,44] and non-uniform intracellular distribution of nanoparticles,

3D-based investigation might aid in mitigating the constraints associated with 2D level and facilitates the "correction" of experimental findings.

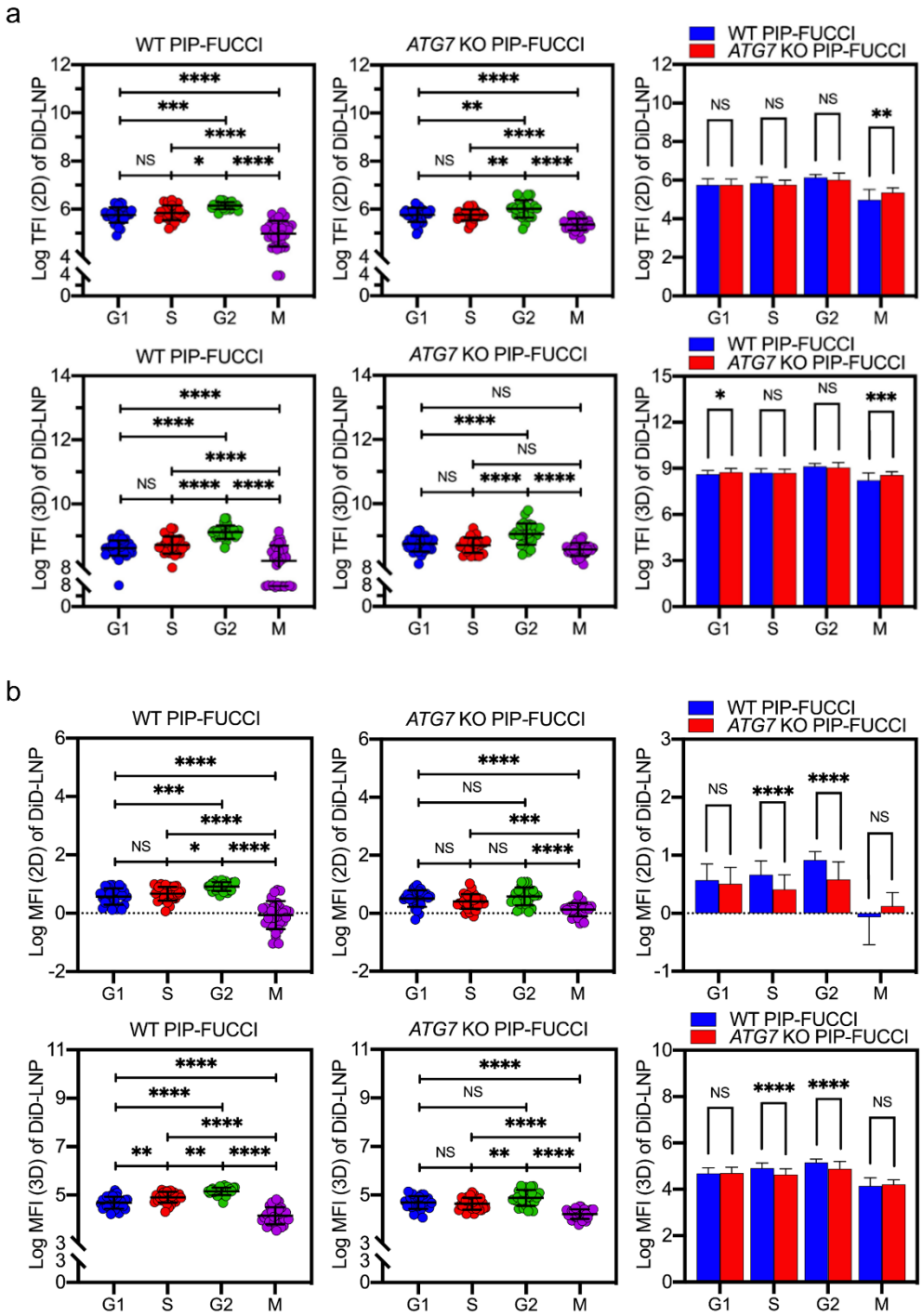

Fig. 5. Determination of cell cycle- and endogenous autophagy-associated cellular uptake of DiD-labelled lipid nanoparticles (DiD-LNP) using the newly established technical platform. a, Statistical analysis of Total Fluorescence Intensity (TFI) in G1-phase, S-phase, G2-phase and M-phase WT and *ATG7* KO PIP-FUCCI cells respectively measured at two-dimensional (2D, upper panel) and three-dimensional (3D, lower panel) levels. **b**, Statistical analysis of Mean Fluorescence Intensity (MFI) in WT and *ATG7* KO PIP-FUCCI cells respectively measured at aforementioned four cell cycle phases, as well as at 2D (upper panel) and 3D (lower panel) levels. WT PIP-FUCCI, wide type U2OS cells stably expressing PIP-FUCCI; *ATG7* KO PIP-FUCCI, *ATG7* knockout U2OS cells stably expressing PIP-FUCCI. DiD-LNP was administered at a dosage equivalent to 6 μg/mL luciferase mRNA

for 2 hours. All data were analyzed after log_{10} transformation and presented as "mean ± standard deviation" (n = 25-30). Statistical analysis of DiD-LIP uptake among four different cell cycle phases was conducted using ANOVA with Bonferroni correction, while differences between WT and *ATG7* KO PIP-FUCCI cell lines were evaluated with an independent sample *t*-test. *, $P < 0.05$; **, $P < 0.01$; ***, $P < 0.001$; ****, $P < 0.0001$. NS, not significant.

Conclusions

Through construction and application of a platform simultaneously overcoming several long-lasting methodological obstacles, we present initial and systematical evidences revealing that G2-phase and M-phase cells respectively have the maximum and minimum uptake of LIP and LNP. Nevertheless, these two distinct cell populations were muddled up together (so called G2/M-phase cells) because of methodological deficiencies in previous studies. Meanwhile, in general, this work demonstrates enhanced nanoparticle uptake by *ATG7* knockout, thereby providing a novel line of supportive evidence for combined use of anticancer modalities with autophagy blockers currently under preclinical and clinical evaluations[50,51]. Although several issues warrant further investigation, e.g. detailed mechanisms mediating cell cycle- and autophagy-associated nanoparticle uptake, merits of TFI and MFI at different dimensional levels, and possible specificity of nanoparticle type, our findings have opened new insights into optimizing the design and application of lipid-based and possibly other nanomedicines besides a valuable technical solution. Particularly, around 3,200 LIP/LNP-based nano-formulations are under clinical investigations.

Table 1. Cell cycle- and autophagy-associated uptake patterns of DiD-LIP and DiD-LNP by cancer cells based on the multi-functional platform

Cell line	Dimension	DiD-LIP		DiD-LNP	
		TFI (a.u.)	MFI (a.u.)	TFI (a.u.)	MFI (a.u.)
WT PIP-FUCCI	2D	M < G1 ≈ S < G2	M < G1 ≈ S ≈ G2	M < G1 ≈ S < G2	M < G1 ≈ S < G2
	3D	M (≈ G1) < (G1 ≈) S < G2	M < G1 ≈ S ≈ G2	M < G1 ≈ S < G2	M < G1 < S < G2
ATG7 KO PIP-FUCCI	2D	M < G1 ≈ S < G2	M < G1 ≈ S ≈G2	M < G1 ≈ S < G2	M < G1 ≈ S ≈ G2
	3D	M < G1 < S < G2	M < G1 ≈ S ≈ G2	M ≈ G1 ≈ S < G2	M < (G1 ≈) S < (G1 ≈) G2

TFI and MFI were first analyzed after $\log_{10}$ transformation. Statistical analysis among four different cell cycle phases was conducted using ANOVA with Bonferroni correction. ≈, no significant difference; TFI, total fluorescence intensity; MFI, mean fluorescence intensity; 2D, two-dimensional level; 3D, three-dimensional level.

References

1. Caster, J. M., Patel, A. N., Zhang, T. & Wang, A. Investigational nanomedicines in 2016: a review of nanotherapeutics currently undergoing clinical trials. *Wires. Nanomed. Nanobi.* **9**, e1416 (2017).

2. Mitchell, M. J. et al. Engineering precision nanoparticles for drug delivery. *Nat. Rev. Drug Discov.* **20**, 101–124 (2021).

3. Yechezkel (Chezy) Barenholz. Doxil® — The first FDA-approved nano-drug: Lessons learned. *J. Control. Release* **160**, 117–134 (2012).

4. Wang, H. Y. et al. Polyethylene glycol (PEG)-associated immune responses triggered by clinically relevant lipid nanoparticles in rats. *NPJ Vaccines* **8**, 169 (2023).

5. Zhivotovsky, B. & Orrenius, S. Cell cycle and cell death in disease: past, present and future. *J. Intern. Med.* **268**, 395–409 (2010).

6. Abouzeid, A. H. & Torchilin, V. P. The role of cell cycle in the efficiency and activity of cancer nanomedicines. *Expert Opin. Drug De.* **10**, 775–786 (2013).

7. Maleki, E. H., Bahrami, A. R. & Matin, M. M. Cancer cell cycle heterogeneity as a critical determinant of therapeutic resistance. *Genes Dis.* **11**, 189–204 (2024).

8. Sui, M. H., Dziadyk, J. M., Zhu, X. M. & Fan, W. M. Cell cycle-dependent antagonistic interactions between paclitaxel and γ-radiation in combination therapy. *Clin. Cancer Res.* **10**, 4848–4857 (2004).

9. Sui, M. H. & Xiong, X. X. Combination of gemcitabine antagonizes antitumor activity of paclitaxel through prevention of mitotic arrest and apoptosis. *Cancer Biol. Ther.* **5**, 1015–1021 (2006).

10. Sui, M. H. et al. G2 checkpoint abrogator abates the antagonistic interaction between antimicrotubule drugs and radiation therapy. *Radiother. Oncol.* **104**, 243–248 (2012).

11. Larson, N. et al. Biodegradable multiblock poly (N-2-hydroxypropyl) methacrylamide gemcitabine and paclitaxel conjugates for ovarian cancer cell combination treatment. *Int. J. Pharm.* **454**, 435-443 (2013).

12. Zhang, R., Yang, J. Y., Sima, M., Zhou, Y. & Kopeček, J. Sequential combination therapy of ovarian cancer with degradable N-(2-hydroxypropyl) methacrylamide copolymer paclitaxel and gemcitabine conjugates. *P. Natl. Acad. Sci. U. S. A.* **111**, 12181-12186 (2014).

13. Zheng, S. et al. Effects of cell cycle on the uptake of water soluble quantum dots by cells. *J. Appl. Phys.* **110**, 124701 (2011).

14. Wu, J. et al. Statistical single-cell analysis of cell cycle-dependent quantum dot cytotoxicity and cellular uptake using microfluidic system. *RSC Adv.* **4**, 24929–24934 (2014).

15. Patel, P. et al. Cell cycle dependent cellular uptake of zinc oxide nanoparticles in human epidermal cells. *Mutagenesis* **31**, 481–490 (2016).

16. Kim, J. A., Åberg, C., Salvati, A. & Dawson, K. A. Role of cell cycle on the cellular uptake and dilution of nanoparticles in a cell population. *Nat. Nanotechnol.* **7**, 62–68 (2012).

17. Go, E. J., Kim, E. J. & Hur, W. *In vitro* cellular uptake of fibroin microspheres and its dependency on the cell cycle stage. *J. Microencapsul.* **30**, 124–131 (2013).
18. Huang, C. et al. Altered cell cycle arrest by multifunctional drug-loaded enzymatically-triggered nanoparticles. *ACS Appl. Mater. Inter.* **8**, 1360–1370 (2016).
19. Tang, J. H. et al. The role of the cell cycle in the cellular uptake of folate-modified poly(L-amino acid) micelles in a cell population. *Nanoscale* **7**, 20397–20404 (2015).
20. Su, L. J. et al. GRP75-driven, cell-cycle-dependent macropinocytosis of Tat/pDNA-Ca2+ nanoparticles underlies distinct gene therapy effect in ovarian cancer. *J. Nanobiotechnol.* **20**, 340 (2022).
21. Li, X. H., He, S. K. & Ma, B. Y. Autophagy and autophagy-related proteins in cancer. *Mol. Cancer* **19**, 12 (2020).
22. Akin, D. et al. A novel ATG4B antagonist inhibits autophagy and has a negative impact on osteosarcoma tumors. *Autophagy* **10**, 2021–2035 (2014).
23. Yang, S. H. et al. Pancreatic cancers require autophagy for tumor growth. *Gene Dev.* **25**, 717–729 (2011).
24. Collier, J. J. et al. Emerging roles of ATG7 in human health and disease. *Embo. Mol. Med.* **13**, e14824 (2021).
25. Manzanares, D. & Ceña, V. Endocytosis: the nanoparticle and submicron nanocompounds gateway into the cell. *Pharmaceutics* **12**, 371 (2020).
26. Birgisdottir, Å. B. & Johansen, T. Autophagy and endocytosis – interconnections and interdependencies. *J. Cell Sci.* **133**, jcs228114 (2020).
27. Zheng, W., Wei, M., Li, S. & Le, W. Nanomaterial-modulated autophagy: underlying mechanisms and functional consequences. *Nanomedicine* **11**, 1417–1430 (2016).
28. Sipos, A. et al. Alveolar epithelial cell processing of nanoparticles activates autophagy and lysosomal exocytosis. *Am. J. Physiol-Lung C.* **315**, L286–L300 (2018).
29. Sipos, A., Kim, K.-J., Sioutas, C. & Crandall, E. D. Evidence for nanoparticle-induced lysosomal dysfunction in lung adenocarcinoma (A549) cells. *Int. J. Mol. Sci.* **20**, 5253 (2019).
30. Fageria, L. et al. Functional autophagic flux regulates AgNP uptake and the internalized nanoparticles determine tumor cell fate by temporally regulating flux. *Int. J. Nanomedicine* **14**, 9063–9076 (2019).
31. Yang, Y. et al. Application and interpretation of current autophagy inhibitors and activators. *Acta Pharmacol. Sin.* **34**, 625–635 (2013).
32. Grant, G. D. et al. Accurate delineation of cell cycle phase transitions in living cells with PIP-FUCCI. *Cell Cycle* **17**, 2496–2516 (2018).
33. Jackman, J. & O'Connor, P. M. Methods for synchronizing cells at specific stages of the cell cycle. *Curr. Protoc. Cell Biol.* **8**, 8.3.1-8.3.20 (1998).
34. Doxil prescribing information. https://www.accessdata.fda.gov/drugsatfda_docs/label/2019/050718s055lbl.pdf (2019).

35. Comirnaty prescribing information. https://labeling.pfizer.com/ShowLabeling.aspx?id=16351&format=pdf (2021).
36. Liu, R. F., Tang, J., Xu, Y. X. & Dai, Z. F. Bioluminescence imaging of inflammation *in vivo* based on bioluminescence and fluorescence resonance energy transfer using nanobubble ultrasound contrast agent. *ACS Nano* **13**, 5124–5132 (2019).
37. Yang, L. et al. Live macrophage-delivered doxorubicin-loaded liposomes effectively treat triple-negative breast cancer. *ACS Nano* **16**, 9799–9809 (2022).
38. Khare, P. et al. Lipid nanoparticle-mediated drug delivery to the brain. *Adv. Drug Deliver Rev.* **197**, 114861 (2023).
39. Cadart, C. et al. Exploring the function of cell shape and size during mitosis. *Dev. Cell* **29**, 159–169 (2014).
40. Kessel, D. H., Price, M. & Reiners, Jr., J. J. ATG7 deficiency suppresses apoptosis and cell death induced by lysosomal photodamage. *Autophagy* **8**, 1333–1341 (2012).
41. Li, W. et al. Phospholipid peroxidation inhibits autophagy via stimulating the delipidation of oxidized LC3-PE. *Redox Biol.* **55**, 102421 (2022).
42. Taubenberger, A.V., Baum, B. & Matthews, H.K. The mechanics of mitotic cell rounding. *Front. Cell Dev. Biol.* **8**, 687 (2020).
43. Needham, D. Possible role of cell cycle-dependent morphology, geometry, and mechanical properties in tumor cell metastasis. *Cell Biophys.* **18**, 99–121 (1991).
44. Wang, Z.X. Regulation of cell cycle progression by growth factor-induced cell signaling. *Cells* **10**, 3327 (2021).
45. Raucher, D. & Sheetz, M. P. Membrane expansion increases endocytosis rate during mitosis. *J. Cell Biol.* **144**, 497–506 (1999).
46. Yang, Y.P. et al. Application and interpretation of current autophagy inhibitors and activators. *Acta Pharmacol. Sin.* **34**, 625-635 (2013).
47. Park, E. J. et al. Chloroquine enhances TRAIL-mediated apoptosis through up-regulation of DR5 by stabilization of mRNA and protein in cancer cells. *Sci. Rep.* **6**, 22921 (2016).
48. Alber, A. B. & Suter, D. M. Dynamics of protein synthesis and degradation through the cell cycle. *Cell Cycle* **18**, 784–794 (2019).
49. Li, Y. et al. APC/CCDH1 synchronizes ribose-5-phosphate levels and DNA synthesis to cell cycle progression. *Nat. Commun.* **10**, 2502 (2019).
50. Zheng, Y., Su, C., Zhao, L. & Shi, Y.J. Chitosan nanoparticle-mediated co-delivery of shAtg-5 and gefitinib synergistically promoted the efficacy of chemotherapeutics through the modulation of autophagy. *J. Nanobiotechnol.* **15**, 28 (2017).
51. Hu, C.L. et al. Co-delivery of the autophagy inhibitor si-Beclin1 and the doxorubicin nano-delivery system for advanced prostate cancer treatment. *J. Biomater. Appl.* **36**, 1317-1331 (2022).

Methods

Major reagents

Cholesterol, 1-palmitoyl-2-stearoyl-sn-glycero-3-phosphocholine (HSPC), 1,2-distearoyl-sn-glycero-3-phosphocholine (DSPC) and 1,2-distearoyl-sn-glycero-3-phosphoethanolamine-N-[methoxy(polyethylene glycol)-2000] ($mPEG_{2000}$-DSPE) were from Lipoid GmbH (Ludwigshafen, Germany). [(4-Hydroxybutyl)azanediyl]di(hexane-6,1-diyl) bis(2-hexyldecanoate) (ALC-0315) and 2-[(polyethylene glycol)-2000]-N,N-ditetradecylacetamide (ALC-0159) were acquired from SINOPEG (Xiamen, China). 1,1′-Dioctadecyl-3,3,3′,3′-tetramethylindotricarbocyanine, 4-chlorobenzenesulfonate salt (DiD) was from MKBio (Shanghai, China). Firefly luciferase mRNA (LUC mRNA) was from Afana Biotechnology (Hefei, China). Ferric chloride hexahydrate and ammonium thiocyanate were from Sigma-Aldrich (St. Louis, MO, USA). Lipofectamine 3000 and Opti-MEM were purchased from Thermo Fisher Scientific (Waltham, MA, USA). Polybrene was from Santa Cruz (Dallas, TX, USA). G418 was from InvivoGen (San Diego, CA, USA). Glutaraldehyde, ethanol and acetone were from Hushi Chemical (Shanghai, China). Lead citrate was from Macklin (Shanghai, China). RIPA buffer and DAPI staining solution were from Beyotime (Shanghai, China). Proteases inhibitor and phosphatase inhibitor were from Yeason (Shanghai, China). Protein marker was from BioRad (Hercules, CA, USA).

Lentivirus concentration kit (Cat. NO. 41101ES50) was acquired from Yeason. BCA protein assay kit (Cat. NO. FD2001) was obtained from Thermo Fisher Scientific. E.Z.N.A. Endo-free plasmid maxi kit (Cat. NO. D6926-03) was from Omega (Norcross, GA, USA). Cell counting kit-8 (Cat. NO. HY-K0301) was from MedChemExpress (Shanghai, China). Plasmids of psPAX2 (Cat. NO. 12260), pMD2.G (Cat. NO. 12259), pLenti-PGK-Neo-PIP-FUCCI (PIP-FUCCI) (Cat. NO. 118616), pLenti PGK Neo DEST (empty vector) (Cat. NO. 19067) and GFP-LC3 (Cat. NO. 11546) were from Addgene (Cambridge, MA, USA).

Anti-ATG7 antibody (Cat. NO. ab133528; clone name, EPR6251) and anti-SQSTM1/p62 antibody (Cat. NO. ab91526) were from Abcam (Waltham, MA, USA). LC3A/B XP Rabbit mAb (Cat. NO. 12741S; clone name, D3U4C) and β-actin antibody (Cat. NO. 4967) were from Cell Signaling Technology (Danvers, MA, USA). EpCAM monoclonal antibody, FITC (Cat. NO. MA1-10197; clone name, VU-1D9), goat anti-rabbit IgG (H+L) highly cross-adsorbed secondary antibody

(Alexa Fluor 488) (Cat. NO. A32731), goat anti-rabbit IgG (H+L) cross-adsorbed secondary antibody (Alexa Fluor 546) (Cat. NO. A11010), and goat anti-mouse IgG (H+L) cross-adsorbed secondary antibody (Alexa Fluor 546) (Cat. NO. A11003) were from Thermo Fisher Scientific.

Cell lines and cell cultures

Wild type (WT) and *ATG7* knockout (*ATG7* KO) human osteosarcoma cancer cell lines U2OS were kind gifts from Professor Qiming Sun at Zhejiang University School of Medicine. Human kidney epithelial cell line 293T was from the Shanghai Institute of Cells, Chinese Academy of Sciences. All cell lines, including newly established WT and *ATG7* KO PIP-FUCCI cell lines (see below section), were authenticated by STR profiling (Tsingke Biotechnology, Beijing, China) and confirmed to be mycoplasma free. All cell lines were in cultured in DMEM supplemented with 10% (v/v) fetal bovine serum and maintained at 37 °C in an atmosphere containing 5% CO_2.

Preparation of model nanoparticles DiD-LIP and DiD-LNP

DiD-LIP was synthesized according to the officially published formulation of Doxil®[34] and previous reports[52]. First, HSPC, cholesterol and $mPEG_{2000}$-DSPE, at 56.6:38.1:5.3 molar ratio, were hydrated in 10 mM sucrose-histidine buffer at pH6.5. Subsequently, DiD was added into the lipid mixture at a concentration of 0.4 mol%, followed by vortex at 60 °C for 2-3 minutes to generate multilamellar vesicles (MLVs). Finally, the MLVs were reduced in size using 400, 100, 80, and 50 nm-pore size polycarbonate filters with a 10-mL extruder barrel (Northern Lipids, Vancouver, Canada), and stored at a temperature of 2-8 °C until use.

DiD-LNP was prepared based on the officially published formulation of Comirnaty®[35] using a modified procedure we previously described[4,53]. Initially, ALC-0315, DSPC, cholesterol and ALC-0159 were dissolved at a molar ratio of 46.3: 9.4: 42.7: 1.6 to fabricate the ethanol phase and DiD was then added into the lipids at a concentration of 0.4 mol%. Meanwhile, LUC mRNA was dissolved in 20 mM citrate buffer to prepare the aqueous phase. Subsequently, the above two phases were mixed with a microfluidic mixer (Precision Nanosystems, Canada) at a flow rate ratio of 1:3 (ethanol: aqueous). Afterwards, the resulting nanoparticle solution was subjected to dialysis against 10 × volume of PBS for at least 18 hours using tangential flow filtration (TFF) membranes with molecular

weight cut-offs of 100 kD (Sartorius Stedim, Germany). With the assistance of an Amicon ultracentrifugal filter (EMD Millipore, Billerica, MA, USA), the nanoparticle solution was passed through a 0.22 μm filter and ultimately concentrated to the desired concentration.

General characterization of DiD-LIP and DiD-LNP

As we previously introduced in details[4], a Zetasizer Nano ZS instrument (Malvern Instruments Ltd, Malvern, UK) was employed to measure hydrodynamic size (Z-average), polydispersity index (PDI) and zeta potential of DiD-LIP and DiD-LNP, with the temperature maintained at 25 °C throughout the testing period. To further evaluate their stability in experimental environment, DiD-LIP and DiD-LNP were diluted with cell culture solution and incubated at 37 °C for 24 hours. Afterwards, nanoparticle samples were respectively collected at specified time points (1 hour, 2 hours, 6 hours, 12 hours and 24 hours post-incubation). Except that the test temperature was changed to 37 °C, samples collected were subjected to aforementioned characterization of Z-average and PDI. Moreover, morphology of DiD-LIP and DiD-LNP was examined with Cryo-TEM, with images captured with a Talos F200C instrument (FEI/Thermo Scientific, Waltham, MA, USA) equipped with a Ceta 4k × 4k camera at an acceleration voltage of 200 kV. Moreover, the phospholipid (HSPC and $mPEG_{2000}$-DSPE) concentration of DiD-LIP solutions and phospholipid (DSPC) concentration of DiD-LNP solutions were determined through Steward's assay as previously described in details[4,54,55]. Eventually, calibration curves were established for DSPC lipids within the range of 25 to 200 μg/mL, and for HSPC lipids within the range of 25 to 150 μg/mL. These curves were applied to determine the ultimate concentrations of phospholipids in the DiD-LIP and DiD-LNP solutions. Three separate experiments were conducted for further statistical analysis. According to previous pharmacokinetics studies and related literatures, the dosages of DiD-LIP and DiD-LNP used in this study were equivalent to 5 μg/mL DOX[34,56,57] and 6 μg/mL LUC mRNA[58-60], respectively. Same volume of PBS was used as a control.

Construction of isogenic WT and *ATG7* KO PIP-FUCCI cell lines stably expressing cell cycle indicator PIP-FUCCI

As previously reported, in the cell cycle indicator plasmid PIP-FUCCI, mVenus fluorescent protein was fused to the PCNA-interacting protein (PIP) degron of human *Cdt1* gene ($Cdt1_{1\text{-}17}$), which is rapidly degraded at the onset of DNA replication[32]. Meanwhile, mCherry fluorescent protein was fused to the *Geminin* gene ($Gem_{1\text{-}110}$), which accumulates during S-phase, G2-phase and M-phase and begins to be degraded at late M-phase[32,61]. Based on these characteristics, Grant et al. demonstrated that in U2OS cell line transfected with PIP-FUCCI, mVenus single-positive cells displaying green nuclear fluorescence are at G1-phase, mCherry single-positive cells displaying red nuclear fluorescence are at S-phase, while mVenus and mCherry double-positive cells displaying yellow (overlap of green and red) nuclear fluorescence are at either G2-phase or M-phase[32].

To take the advantage of cell cycle indicating capability of PIP-FUCCI plasmid in living cells, hereby WT and *ATG7* KO U2OS cell lines were stably transfected with PIP-FUCCI. Briefly, 1×10^6 293T cells were cultured into a 10-cm dish for overnight incubation. For lentiviral transduction, Lipofectamine 3000 was used to co-transfect PIP-FUCCI plasmid, psPAX2 and pMD2.G plasmids into 293T cells, with empty vector serving as a negative control. The medium was replaced 6-8 hours after transfection, and was harvested and concentrated at 72 hours post-transfection. Afterwards, approximately 6×10^4 exponentially growing WT and *ATG7* KO U2OS cells were respectively seeded into cell culture plates. After overnight incubation, cells were exposed to concentrated lentiviral supernatant containing either PIP-FUCCI or empty vector, along with 8 μg/mL polybrene. Transduced cells were then selected for around one week with 500 μg/mL of G418. WT and *ATG7* KO U2OS cells expressing the empty vector, so called WT and *ATG7* KO Vector cell lines respectively, were amplified for subsequent experiments, while those transfected with PIP-FUCCI were sorted by BD FACSAria II flow cytometry (BD Biosciences, CA, USA) to obtain WT and *ATG7* KO PIP-FUCCI cell lines exhibiting strong mVenus and/or mCherry fluorescence for further studies.

It should be noted that PIP-FUCCI transfection alone is hard to distinguish between G2-phase and M-phase cells cultured or growing together. Fortunately, unique properties of typical M-phase cells, e.g. spherical shape and significantly decreased adhesion capability[39], allow for convenient separation of M-phase cells through gentle mitotic shake-off[33], through which a complete distinguishment of four cell cycle phases was successfully achieved by integrating PIP-FUCCI with mitotic shake-off in this study (see below section).

Evaluation of the influence of PIP-FUCCI transfection on cell morphology and proliferation

WT and *ATG7* KO Vector cell lines, as well as WT and *ATG7* KO PIP-FUCCI cell lines were carefully checked with light microscope for morphological examination. In addition, these cell lines were respectively seeded into 6-well plates (1×10^5 cells for each well). A Countess II FL Automated Cell Counter (Thermo Fisher Scientific) was employed for five consecutive cell number counting between 24 hours and 120 hours after seeding, with a 24-hour interval. Cell doubling time of each cell line was calculated according to the following equation: Doubling time = Duration time of cell culture × log (2)/[log (final cell number) – log (initial cell number)].

Flow cytometry to explore possible effects of nanoparticles on cell cycle progression

Exponentially growing WT and *ATG7* KO PIP-FUCCI cells were seeded at 3×10^5 cells per well into 6-well plates and cultured overnight. Cells were then respectively administered with DiD-LIP and DiD-LNP for 2 hours. Afterwards, cells were harvested with trypsinization, rinsed three times with PBS and resuspended in 500 μL of DAPI staining solution. Subsequently, cell cycle progression was analyzed with a CytoFLEX LX (Beckman Coulter, Indianapolis, USA). DAPI, mVenus and mCherry channels were respectively excited with 375 nm, 488 nm and 561 nm lasers, and detected with corresponding 450/45 nm, 525/40 nm and 610/20 nm bandpass filters. As described above, cancer cells exhibited the following cell cycle-dependent fluorescence: G1-phase (mVenus positive), green fluorescence; S-phase (mCherry positive), red fluorescence; G2-phase and M-phase (mVenus and mCherry double-positive), yellow fluorescence.

Examination of possible effects of nanoparticles on autophagic vesicle formation with TEM

Exponentially growing WT and *ATG7* KO PIP-FUCCI cells were seeded at 7×10^5 cells per 6-cm culture dish for overnight incubation. Cells were then respectively administered with DiD-LIP and DiD-LNP for 2 hours. Following overnight fixation with 2.5% glutaraldehyde, cells underwent three washes with PBS for a duration of 10 minutes each. Subsequently, cells were subjected to fixation with 1% osmium tetroxide for 1 hour, followed by rinsing with PBS prior to staining with 2% uranyl acetate for 30 minutes. For dehydration, samples were respectively placed in 50%, 70%, 90% and

100% ethanol for 15 minutes and then in 100% acetone for 20 minutes twice. Afterwards, a Leica UC7 microtome (Leica, Solms, Germany) was used to prepare ultrathin sections and sample staining were performed with lead citrate and uranyl acetate. Photographs of autophagic vesicles were captured using a Tecnai 10 TEM (Philips, Amsterdam, Netherlands) at 100 kV. At least 10 cells were randomly chosen from each group for imaging and statistical analysis.

Western blotting to assess possible effects of nanoparticles on autophagy-related proteins

Exponentially growing WT and *ATG7* KO PIP-FUCCI cells were seeded at 7×10^5 cells per 6-cm culture dish for overnight incubation. Cells were then respectively administered with DiD-LIP and DiD-LNP for 2 hours. Then cells were harvested with trypsinization, rinsed three times with PBS and subjected to RIPA buffer containing proteases and phosphatase inhibitors on ice for 10 minutes. Subsequently, the supernatant was collected through centrifugation at 12,000 × g for 20 minutes. Protein concentrations were determined with a BCA protein assay kit. A gel of 15% SDS-PAGE was used to electrophorese proteins (40 μg /lane) prior to being transferred onto a PVDF membrane. After blocking with 5% (w/v) bovine serum albumin for 1 hour, the membranes were incubated with following antibodies overnight at 4 °C: anti-ATG7 (1:1,000 dilution), anti-SQSTM1/p62 (1:1,000 dilution), anti-MAP1LC3A/B (1:1,000 dilution) and anti-β-actin (1:5,000 dilution). Next, membranes were rinsed with TBS solution containing 0.1% (v/v) Tween 20 and incubated with corresponding secondary antibodies (1:5,000 dilution) for 2 hours. Odyssey imaging system was employed for WB imaging (LI-COR Biosciences, Lincoln, USA).

Integration of PIP-FUCCI expression with mitotic shake-off for complete cell cycle phase separation and scatheless determination of cell cycle-associated nanoparticle uptake

Approximately 8×10^4 exponentially growing WT and *ATG7* KO PIP-FUCCI cells were seeded into confocal dishes for overnight incubation. Then cells were administered with DiD-labelled model nanoparticles (blue intracellular fluorescence in CLSM) at designated dosages and incubated for 1.5 hours. Afterwards, cells were incubated with 25 μL FITC-EpCAM monoclonal antibody for additional 30 minutes to draw the outline of cell membrane (green cell membrane fluorescence in CLSM) and meanwhile exclude apoptotic cells or cell debris.

To achieve complete and scatheless separation of four different cell cycle phases, cells cultured in confocal dishes were gently shaken (so called mitotic shake-off), and the culture medium containing floating mitotic cells was harvested for isolation and transfer of M-phase cells into another new confocal dish. Both the adherent G1-phase (mVenus single-positive, green nuclear fluorescence in CLSM), S-phase (mCherry single-positive, red nuclear fluorescence in CLSM) and G2-pahse (mVenus and mCherry double-positive, yellow nuclear fluorescence in CLSM) cells remained in original confocal dishes, and the floating M-phase cells (mVenus and mCherry double-positive, yellow nuclear fluorescence in CLSM) harvested separately via mitotic shake-off into new dishes were gently rinsed three times with PBS to remove unbound fluoroprobes, before examination with high-resolution CLSM and 3D reconstruction technique (see below section). It is noteworthy that although the emission wavelength of FITC is partially overlapped with that of mVenus, FITC-labeled EpCAM expresses on the cell membrane as an epithelial cell adhesion molecule[62], whereas mVenus expresses in the nucleus[32]. Consequently, there is no interference between them due to distinct expression locations.

High-resolution CLSM and 3D reconstruction technique for multi-dimensional evaluation of cell cycle- and autophagy-associated nanoparticle uptake

Successful construction of WT and *ATG7* KO PIP-FUCCI cell lines and achievement of complete cell cycle phase separation have provided us with the opportunity to simultaneously determine cell cycle- and autophagy-associated cellular uptake of DiD-labelled model nanoparticles. Live-cell imaging was conducted using the Confocal Zeiss LSM 880 (Carl Zeiss, Jena, Germany) equipped with a 63 × oil immersion objective (1.40 NA) with a resolution of 2048 × 2048 pixels, together with an incubation chamber set at 37 °C and 5% CO_2. Filter sets were as follows: mVenus (excitation: 514 nm, emission: 519–590 nm), mCherry (excitation: 561 nm, emission: 570–620 nm), DiD (excitation: 633 nm, emission: 638–756 nm) and FITC (excitation: 488 nm, emission: 500–550 nm)[32]. In addition to labelling cell membrane with FITC, morphological examination of cell with bright field was helpful in identifying typical and healthy M-phase cells with intact and smooth cell membranes.

Besides regular two-dimensional (2D) CLSM imaging to determine the nanoparticle uptake, three-dimensional (3D) imaging was also conducted by acquiring 30-80 μm z-stacks at z-step

intervals of 0.4-1 μm. Total fluorescence intensity (TFI) of intracellular DiD at the 2D level, so called TFI (2D), was measured using Fiji/Image J (imagej.nih.gov). To eliminate variations in TFI (2D) due to differences in cell area, mean fluorescence intensity (MFI) of intracellular DiD at the 2D level, so called MFI (2D), was calculated as the ratio of TFI (2D) vs. cell area[63]. Imaris software (Bitplane) was used to reconstruct 3D images of confocal z-stacks, so that the TFI of intracellular DiD at the 3D level, named as TFI(3D), as well as cell volume could be determined. Similarly, to eliminate variations in TFI (3D) due to differences in cell volume, TFI (3D) was divided by corresponding cell volume to obtain MFI (3D)[64].

Data presentation and statistical analysis

Data were presented as "mean ± standard deviation". Shapiro-Wilk test was used to evaluate normality, while Levene's test was conducted to assess homogeneity of variance. One-way analysis of variance (ANOVA) with Bonferroni correction was conducted for analyzing possible changes on nanoparticle stability and cell cycle progression. Mann-Whitney U test was employed to analyze statistical differences in autophagic vesicle number among various groups. In addition, data including cell area, cell volume, TFI and MFI of DiD-LIP/DiD-LNP at different dimensional levels were first analyzed after $\log_{10}$ transformation. Then their differences among the G1-phase, S-phase, G2-phase and M-phase were conducted using ANOVA with Bonferroni correction, while their differences between WT and *ATG7* KO PIP-FUCCI cell lines were evaluated with an independent sample t-test. Pearson correlation coefficients were employed to evaluate the correlations among multi-dimensional TFI and MFI. All statistical analyses were conducted using SPSS 21.0 (IBM SPSS, Chicago, USA). $P < 0.05$ is considered statistically significant.

References

52. Bavli, Y. et al. Doxebo (doxorubicin-free Doxil-like liposomes) is safe to use as a pre-treatment to prevent infusion reactions to PEGylated nanodrugs. *J. Control. Release* **306,** 138–148 (2019).
53. Zhang, N. N. et al. A Thermostable mRNA Vaccine against COVID-19. *Cell* **182**, 1271-1283. (2020).
54. Stewart, J. C. M. Colorimetric determination of phospholipids with ammonium ferrothiocyanate. *Anal. Biochem.* **104**, 10–14 (1980).

55. Bandyopadhyay, A., McCarthy, K. A., Kelly, M. A. & Gao, J. Targeting bacteria via iminoboronate chemistry of amine-presenting lipids. *Nat. Commun.* **6**, 6561 (2015).
56. Li, Y. J. et al. Thermal-responsive carbon monoxide (CO) delivery expedites metabolic exhaustion of cancer cells toward reversal of chemotherapy resistance. *ACS Central Sci.* **5**, 1044-1058 (2019).
57. Shi, C.Y. et al. A drug-specific nanocarrier design for efficient anticancer therapy. *Nat. Commun.* **6**, 7449 (2015).
58. Parhiz, H. et al. PECAM-1 directed re-targeting of exogenous mRNA providing two orders of magnitude enhancement of vascular delivery and expression in lungs independent of apolipoprotein E-mediated uptake. *J. Control. Release* **291**, 106-115 (2018).
59. Paunovska, K. et al. Increased PIP3 activity blocks nanoparticle mRNA delivery. *Sci. Adv.* **6**, 5672 (2020).
60. Maugeri, M. et al. Linkage between endosomal escape of LNP-mRNA and loading into EVs for transport to other cells. *Nat. Commun.* **10**, 4333 (2019).
61. McGarry, T. J. & Kirschner, M. W. Geminin, an inhibitor of DNA replication, is degraded during mitosis. *Cell* **93**, 1043–1053 (1998).
62. Jing, Y. Y. et al. Quantitatively mapping the assembly pattern of EpCAM on cell membranes with peptide probes. *Anal. Chem.* **92**, 1865–1873 (2020).
63. Shen, X. et al. MiR-322/-503 rescues myoblast defects in myotonic dystrophy type 1 cell model by targeting CUG repeats. *Cell Death Dis.* **11**, 891 (2020).
64. Trivedi, P. et al. The inner centromere is a biomolecular condensate scaffolded by the chromosomal passenger complex. *Nat. Cell Biol.* **21**, 1127–1137 (2019).

Acknowledgments

This work was supported by grants from the National Natural Science Foundation of China (21722405 and 22075243 to Dr. Meihua Sui), Zhejiang Provincial Natural Science Foundation of China (LZ23E030003 to Dr. Meihua Sui) and Startup Foundation for Hundred-Talent Program of Zhejiang University (to Dr. Meihua Sui). In addition, we would like to acknowledge Shenghai Chang, Lingyun Wu and Beibei Wang in the Center of Cryo-Electron Microscopy (CCEM), Zhejiang University for their technical assistance on Cryo-EM and TEM. We would like to acknowledge Shuangshuang Liu, Guifeng Xiao and Yueting Xing from the Core Facilities, Zhejiang University School of Medicine for their technical assistance on confocal live imaging, 3D reconstruction and flow cytometry. We would also like to acknowledge Yina Wang for her assistance on language polishing.

Author contributions

M.S., the principal investigator of the major supporting grants, and Y.W. conceived the study and defined the goals of the present study. M.S., Y.W., G.L. and H.W. designed the experiments. Y.W., G.L. and H.W. performed the research. M.S., Y.W., G.L., H.W., Y.Z., W.Z., J.L. and B.C. discussed this project and analyzed the data. M.S., Y.W., G.L. and H.W. drafted the manuscript. M.S., Y.W., G.L., H.W., Y.Z., W.Z., J.L. and B.C. revised and edited the manuscript. These authors contributed equally: Y.W., G.L. and H.W.

Competing interests

The authors declare no competing interests.

Correspondence and requests for materials should be addressed to Meihua Sui.